Anisotropic Generation and Detection of Surface Plasmon Polaritons Using Near-Field Apertured Probes

Juan M. Merlo, *Member, IEEE*, Charlotte Rhoads, and Madeleine Hoag Carhart

***Abstract*—Most recent studies centered on light-matter interactions at the nanoscale rely on near-field microscopy. Despite this, few works have been reported to date regarding the anisotropic generation of surface plasmons polaritons on metallic surfaces. This phenomenon is attributed exclusively to scattering near-field probes. This work is dedicated to demonstrating that the anisotropic generation of surface plasmons polaritons is not exclusive to scattering probes. Using a near-field apertured probe, in collection mode, we demonstrate the generation and detection of such phenomenon. By analyzing the momentum components of the obtained near-field images, it is demonstrated that the detected signal is mostly composed of near-field components. Therefore, our approach reduces the contribution of propagating modes, consequently easing the interpretation of near-field images.**

***Index Terms*—Surface plasmon polaritons, near-field microscopy, surface characterization, apertured probes.**

I. Introduction

SURFACE plasmon polaritons (SPPs) are the cumulative oscillations of electrons in a metal-dielectric interface (MDI) [1]. Due to their nature, SPPs are strongly confined to the MDI where they are excited at [1]. Actually, this property has allowed SPPs to find applications in sensing devices [2], [3], waveguides [4], [5], and communication systems [6], [7], among others [8], [9], [10], [11], [12], [13]. In addition, the SPPs confinement imposes an important constraint to their observation, i.e., it needs special techniques to retrieve the information at the MDI. The techniques used most for the SPPs observation are the leakage radiation microscopy (LRM) [14], [15] and near-field microscopy (NFM) [4], [6]. The LRM is based on the continuity of the in-plane component of the SPPs momentum at the MDI, and its coupling to the far-field by an optical system, when the metal layer supporting the SPPs is thin enough to allow symmetric and asymmetric modes to hybridize [14]. Even when LRM can be used for the quantitative observation of the SPPs propagation, this technique possesses a critical disadvantage which is the observation is still limited by the classical resolution limit [14].

Manuscript received 13 May 2023; revised 10 August 2023; accepted 26 August 2023. Date of publication 29 August 2023; date of current version 8 September 2023. This work was supported in part by Vassar College under the startup number ST000057 and in part by the Lucy Maynard Salmon Research Fund. *(Corresponding author: Juan M. Merlo.)*

The authors are with the Physics and Astronomy Department, Vassar College, Poughkeepsie, NY 12604 USA (e-mail: jmerloramirez@vassar.edu; crhoads@vassar.edu; mcarhart@vassar.edu).

Digital Object Identifier 10.1109/JPHOT.2023.3309890

On the other hand, NFM is based on the raster scanning of a sharp probe over the MDI. Such a probe scatters the SPPs electromagnetic field to be detected by using an optical fiber [6] or a free-space optical system [16], [17]. In the first case, the near-field probes are made of an optical fiber sharpened at its extreme end and coated with a metallic layer in such a way that it has an aperture that senses the near-field intensity [4], [6]. These kinds of probes are usually called apertured probes (APs) [4]. In the second case, the probe is usually a silicon tip with a metallic coating that scatters the near-field to be detected in the far-field by an optical system that functions as illumination and detection [17]. These probes are commonly called scattering probes and have provided high resolution imaging of SPPs phenomena [16].

It is important to know that NFM has the ability to simultaneously image the topography of the sample and the near-field interactions, providing the opportunity to relate the electromagnetic interactions with the characteristics of the sample surface topography [4]. Furthermore, using NFM one can obtain images without the effect of the classical resolution limit as the near-field probes usually have sizes ranging from tens to hundreds of nanometers [4], [16]. Such a size actually determines the resolution of a near-field microscope [6].

On the other hand, it was recently suggested that the generation of SPPs by scattering near-field probes is an anisotropic process due to several excitation and detection channels [18], [19]. Although a natural assumption could be that the APs can generate and detect such anisotropy, there is no evidence to date of a study of this kind. In this work, we demonstrate that the anisotropic generation of SPPs can be achieved using APs. A systematic study allowed us to conclude that it is possible to obtain similar results to those already published [18], [19]. The presented results are important for the generalization of the study of SPPs interactions on a MDI, independently of the way they are generated and measured.

II. Experimental Methods

A. Near-Field Imaging

The imaging of the SPPs intensity was made by using a near-field scanning optical microscope (NSOM, Nanonics Multiview 1500) in collection mode with an AP of $\sim$ 300 nm diameter. The number of points in each image was adjusted in such a way that the step size was kept constant to 25 nm. The near-field probe and the excitation spot were at a fixed position while the scanning

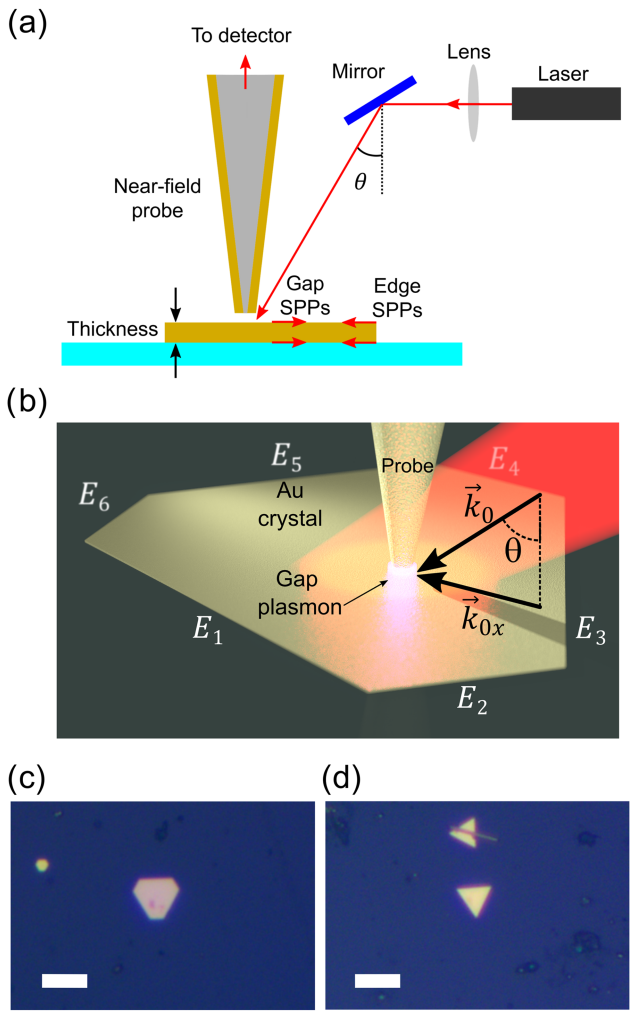

Fig. 1. (a) Schematic representation of the experimental setup. (b) Artistic closeup of the experimental setup in the crystal. The vectors are not on the correct scale. Optical images of Au crystals with hexagonal (c) and triangular (d) symmetries. The scale bar represents 50 μm in both cases.

was performed by the sample. A laser source in p-polarization was used to excite the SPPs. The excitation wavelength was 660 nm, and the incidence angle (θ) was 32° ± 2° with respect to the normal of the sample surface for convenience in our experimental setup. The incident beam was focused on a spot of ∼ 5 μm diameter, centered at the tip of the near-field probe. Fig. 1(a) shows a schematic representation of our experimental setup and Fig. 1(b) shows a closeup of the crystal and the definition of the in-plane component of the incident field.

B. Sample Fabrication

The samples consisted of a set of single crystal Au flakes fabricated by chemical reduction [20] deposited on glass substrates. It is important to note that we used single crystal Au flakes for our study due to their important role in the study and implementation of modern plasmonics applications [21], [22], [23], and for comparison purposes [19]. Although the crystal phase was not characterized, we assumed the resulting flakes have the same nature as those previously reported [20].

Our fabrication procedure can be described as follows. We used glass substrates, 25 × 25 mm^2 and 1 mm thick, that were cleaned by an ultrasonic bath in isopropyl alcohol followed by acetone, for 10 minutes each, and dried with clean air for 10 seconds. For the Au crystal fabrication, we used 20 μl of $HAuCl_4$ dissolved in 20 ml of ethylene glycol. The solution, with two substrates immersed in, was heated to ∼70 °C for 12 hours. At the end of the processing time, the glass substrates were removed from the solution, washed in deionized water for 1 minute, followed by acetone bath for 3 minutes, and dried with clean air for 30 seconds. This fabrication proved to be the most reliable in our experimental conditions. Although the crystal orientation was not determined, it has been demonstrated that under similar experimental conditions to ours, the results were quite similar. As such, we are confident that the crystal orientation of our samples was {111} at the studied surface [19], [20]. Fig. 1(c) and (d) show optical images of a set of fabricated crystals with the same shapes as the reported for near-field microscopy.

III. Results

It was found that the grown crystals displayed triangular and hexagonal shapes, see Fig. 1(c) and (d), as expected [20]. Their transverse dimensions ranged from 1 μm to 50 μm and their thickness ranged from 30 nm to 80 nm. In this sense, we selected the crystals that allowed us to observe the propagation of SPPs over the surface of the crystals, meaning the selected sides were larger than 10 μm. In addition, in order to ensure the existence of SPPs on the flat surface of the Au flakes, we selected the crystals with thicknesses of 35 nm and larger [1].

Fig. 2(a) shows the topography of one Au crystal flake with triangular geometry. It is clear that the height of this crystal accomplished our targeted thickness. The inset shows a height profile taken in the dashed line. It is well-known that the surface of Au flakes is smooth due to their atomic structure [19], [20]. However, the difference in the height observed in Fig. 2(a) over the surface of the Au flake was due to the scanning effects of the NFM. We have identified the edges E1, E2, and E3 in order to facilitate the discussion of the nature of the SPPs interactions.

A near-field intensity image was simultaneously acquired to the topography, Fig. 2(a), and it is shown in Fig. 2(b). In this case, it was possible to see that an interference pattern was generated by the interaction of SPPs with different momenta, particularly in the perpendicular directions to the edges E1 and E2. This was an expected result as in addition to the radially symmetric SPPs generated by the AP, the presence of the crystal edges also matched the momentum conditions for SPPs generation [1], [22]. In addition, it is easy to distinguish a low-frequency modulation of the intensity perpendicular to E1, E2, and E3 corresponding to the in-plane component of the incident field, $\vec{k}_{0x}$ in Fig. 1(b). This was interesting in particular for the case of E3, as although it did not support the generation of SPPs, probably due to its crystal orientation [20], it still scattered the in-plane component of the incident field. This was an expected result due to the presence of such an edge. The same explanation applies for

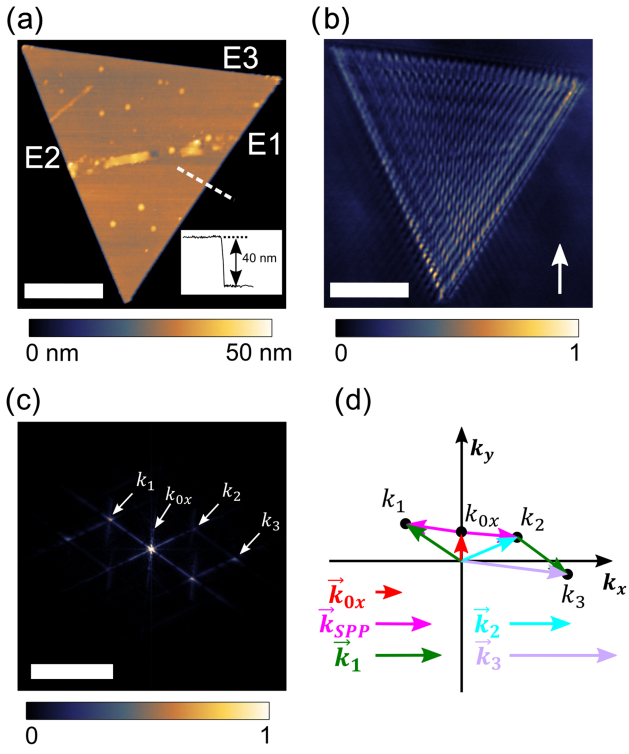

Fig. 2. (a) Topography of a single crystal Au flake. The inset shows the height profile taken in the dashed line. (b) Normalized near-field intensity simultaneously registered with (a). The white arrow represents the direction of the in-plane component of the incident field. In both cases, the scale bar represents 10 μm. (c) Normalized 2D-FFT of the near-field intensity reported in (b). The scale bar represents 10 μm^{-1}. (d) Schematic representation of the momentum components in the 2D-FFT shown in (c); the scale has been changed for better visualization. The names and sizes of each momentum are shown as inset to this scheme.

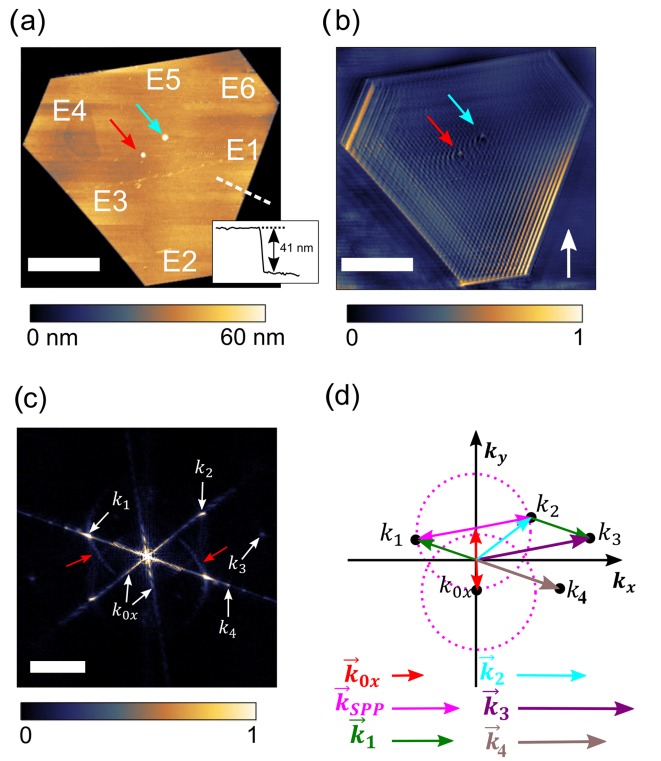

Fig. 3. (a) Topography of a single crystal Au flake with hexagonal symmetry. The inset shows the height profile taken in the dashed line. (b) Normalized near-field intensity simultaneously registered with (a). The white arrow represents the direction of the in-plane component of the incident field. In both cases, the scale bar represents 10 μm. (c) Normalized 2D-FFT of the near-field intensity reported in (b). The scale bar represents 10 μm^{-1}. (d) Schematic representation of the momentum components in the 2D-FFT shown in (c). The names and sizes of each momentum are shown as inset to this scheme.

E1 and E2. It is also important to mention the anisotropy in the SPPs interference. It was due to two factors, the illumination angle, from a single side of the probe, and the direction of the crystal edges. This has already been demonstrated in SPPs generation but using scattering probes [18], [19].

Although the near-field images can provide important information about the SPPs propagation and interactions on the surface of the Au crystal, it is necessary to analyze the momentum space to determine the spatial-frequency components of the field. A two-dimensional fast Fourier transform (2D-FFT) was performed on the near-field image, Fig. 2(b), and the result is shown in Fig. 2(c). It should be pointed out that the advantage of calculating the 2D-FFT was that all the momentum components became visible at once. This improved the analysis of the SPPs interactions on the surface of the Au crystal, in comparison with the method presented in reference 19. In our case, the size of each momentum component was determined by the scale at the Fourier space. From Fig. 2(c), it is clear that there are four main components in the momentum space, i.e., $\vec{k}_{0x}$, $\vec{k}_1$, $\vec{k}_2$, and $\vec{k}_3$, see the white arrows. Actually, from Fig. 2(c), the component $\vec{k}_{0x}$ was visible in perpendicular directions to the Au crystal edges, meaning the in-plane component of the incident field was scattered by the edges of the Au crystal, interacted with the SPPs, and detected by the near-field probe, as mentioned before. Moreover, the low-frequency pattern observed in Fig. 2(b) was a result of this interaction.

In order to simplify the visualization of the momentum space, we present its schematic representation in Fig. 2(d). In this way, it is quite simple to see that the components $\vec{k}_1$ and $\vec{k}_2$ were generated by the displacement of $\vec{k}_{SPP}$ — the SPP momentum in the flat surface of the Au crystal — by $\vec{k}_{0x}$, the in-plane component of the incident field, in other terms, $\vec{k}_i = \vec{k}_{0x} + \vec{k}_{SPP}$ with $i = 1, 2$, see Fig. 2(d). In addition, using this scheme, we could determine that the $\vec{k}_3$ component was simply $\vec{k}_3 = \vec{k}_1 + \vec{k}_2$, or simply the interference between $\vec{k}_1$ and $\vec{k}_2$. In contrast, it was possible to observe that the edge E3 did not generate SPPs as E1 and E2. We believe this happened due to the momentum mismatch in such an edge as has been observed elsewhere [22], i.e., the orientation of the crystal edge suppressed both the generation and reflection of SPPs, as mentioned before.

In order to extend our findings, we report a second crystal with hexagonal symmetry. In such a case, the topographic image, Fig. 3(a), demonstrated a similar thickness to that reported in the previous case, Fig. 2. As before, the artifact in the height was due to the scanning process. In this case, we have identified each of the edges as Ei, with $i = 1$ to 6. In addition to the hexagonal symmetry, we selected the crystal because it also had a clear pair of particles on its surface, see red and cyan arrows in Fig. 3(a);

the reason for this selection will be clear later. We believe that these particles are the seeds of new layers in the crystal [20].

As before, a near-field image was simultaneously acquired with the topography. Fig. 3(b) displays the normalized near-field intensity. It is clear that the interference patterns generated by the interaction of SPPs with different momenta was measured as in the previous case. Moreover, in this case, it is possible to observe the presence of SPPs patterns generated by edges E1, E2, E3, and E4. We could observe that the particles on the surface of the Au crystal, see red and cyan arrows in Fig. 3(a), were clearly visible in the near-field image, see the red and cyan arrows in Fig. 3(b). Moreover, both particles matched the conditions to scatter the SPPs as in-plane waves as it is checked by the weak concentric ring generated around each of the particles, see Fig. 3(b). Actually, this feature is a clear signature of the concentric nature of the SPPs launched by the near-field probe generated by an in-plane field $\vec{k}_{0x}$, a commonly acknowledged fact for scattering probes [17], [18], [19]. The existence of the anisotropy in the SPPs patterns was due to the aforementioned factors as the experimental conditions were the same.

As in the previous case, we performed the 2D-FFT of the near-field image, see Fig. 3(c). This time, we found a richer momentum space, with five components $\vec{k}_i$, with $i = 1$ to 4, and $\vec{k}_{0x}$. In addition, the momentum space showed two circularly symmetric rings due to the presence of the Au particles on the crystal surface, see the red arrows in Fig. 3(c). Once again, the existence of components perpendicular to each edge with sizes $|\vec{k}_{0x}|$, confirmed our previous explanation regarding the interactions and detection of the scattering of the in-plane component of the incident field, $\vec{k}_{0x}$. Also, we observed the components $\vec{k}_1$, $\vec{k}_2$, and $\vec{k}_3$, as expected from the previous case. Interestingly, we found the existence of $\vec{k}_4$ that was related to the SPPs momentum in the Au-glass interface. This is an important finding as this represents the hybridization of the SPPs modes in the top and bottom surfaces of the Au crystal due to its thickness [1]. Furthermore, $\vec{k}_4$ was only generated by edges E1 and E4. This was likely due to the nature of such edges and their ability to match and reflect the SPPs momentum [22].

Again, we made a schematic representation of the momentum space, and it is shown in Fig. 3(d). In this scheme, we were able to see that, as above, $\vec{k}_i = \vec{k}_{0x} + \vec{k}_{SPP}$ with $i = 1, 2$, and $\vec{k}_3 = \vec{k}_1 + \vec{k}_2$. It is clear that $\vec{k}_4$ is parallel to $\vec{k}_1$, however, it is related to the SPPs modes in the Au-glass interface as mentioned before. Finally, we included the indication of the semi-rings that are visible in Fig. 3(c) as dashed circles in Fig. 3(d). It is clear that these semi-rings have radii equal to $|\vec{k}_{SPP}|$, centered at $\vec{k}_{0x}$. This evidence further supports that $\vec{k}_i = \vec{k}_{0x} + \vec{k}_{SPP}$ with $i = 1, 2$, as we mentioned before and the circular shape of the launched SPPs by the AP.

IV. Discussion

It is important to mention that we could not find any evidence of the contribution of far-field components to our near-field images. This means that APs suppressed the detection of far-field components, resulting in an easier interpretation of the near-field images, with respect to scattering based near-field microscopes [18], [19]. Unfortunately, there is a tradeoff when using APs; although APs provide a straightforward interpretation of the near-field images, the resolution becomes limited, due to the size of the used apertures [6]. This could become an important issue when another kind of surface waves are studied, for example, propagating modes in two-dimensional materials with hyperbolic dielectric functions [24]. In addition, APs probes could present important asymmetries in their geometry, generating important artifacts in the detection of the near-field intensity. It is also important to mention that in the present configuration, the SPPs were generated by a gap plasmon [1] that is dependent on the sizes of the probe and gap between the AP and the sample surface. This generated a deterioration of the resolution, as mentioned above, but at an increased signal to noise ratio. The actual analysis of this gap plasmon due to APs is the matter of a work in progress and will be reported in an independent study.

V. Conclusion

In conclusion, we have shown that the anisotropic generation and detection of SPPs in Au crystal flakes are not exclusive to scattering probes. Actually, using APs a gap plasmon is responsible for this generation of SPPs. It was also verified that the vector analysis of the momentum space allowed the identification of the momenta contained in the near-field images. Finally, although there must be caution in the use of APs, our work opens the possibility for using near-field probes of any kind for the study of SPPs under any conditions of illumination and symmetry of the samples under study.

References

[1] H. Raether, *Surface Plasmons on Surfaces of Small Roughness*. Berlin, Germany: Springer, 1988.

[2] C. Lee, B. Lawrie, R. Pooser, K. G. Lee, C. Rockstuhl, and M. Tame, "Quantum plasmonic sensors," *Chem. Rev.*, no. 121, pp. 4743–4804, 2021.

[3] W. Fan, B. J. Lawrie, and R. C. Pooser, "Quantum plasmonic sensing," *Phys. Rev. A*, vol. 92, 2015, Art. no. 053812.

[4] J. M. Merlo, F. Ye, B. Rizal, M. J. Burns, and M. J. Naughton, "Nearfield observation of light propagation in nanocoax waveguides," *Opt. Exp.*, vol. 22, pp. 14148–14154, 2014.

[5] Y. M. Calm et al., "Optical confinement in the nanocoax: Coupling to the fundamental TEM-like mode," *Opt. Exp.*, vol. 28, pp. 32152–32164, 2020.

[6] J. M. Merlo et al., "Wireless communication system via nanoscale plasmonic antennas," *Sci. Rep.*, vol. 6, 2016, Art. no. 31710.

[7] G. Bellanca, G. Calò, A. E. Kaplan, P. Bassi, and V. Petruzzelli, "Integrated Vivaldi plasmonic antenna for wireless on-chip optical communications," *Opt. Exp.*, vol. 25, pp. 16214–16227, 2017.

[8] A. M. Shrivastav, U. Cvelbar, and I. Abdulhalim, "A comprehensive review on plasmonic-based biosensors used in viral diagnostics," *Commun. Biol.*, vol. 4, 2020, Art. no. 70.

[9] C. E. Garcia-Ortiz, S. Kumar, and S. I. Bozhevolnyi, "Local excitation of surface plasmon polaritons using nitrogen-vacancy centers," *Opt. Lett.*, vol. 40, 2015, Art. no. 3830.

[10] R. Sundararaman et al., "Plasmonics in argentene," *Phys. Rev. Mater.*, vol. 4, 2020, Art. no. 07401.

[11] Y. Wang, X. Shi, T. Oshikiri, S. Zu, K. Ueno, and H. Misawa, "Plasmon induced electron injection into the large negative potential conduction band of Ga_2O_3 for coupling with water oxidation," *Nanoscale*, vol. 12, pp. 22674–22679, 2020.

[12] M. L. Brongersma, N. J. Halas, and P. Nordlander, "Plasmon-induced hot carrier science and technology," *Nature Nanotechnol.*, vol. 10, pp. 25–34, 2015.

[13] J. M. Fitzgerald, S. Azadi, and V. Giannini, "Quantum plasmonic nanoantennas," *Phys. Rev.*, vol. 95, 2017, Art. no. 235414.
[14] A. Hohenau et al., "Surface plasmon leakage radiation microscopy at the diffraction limit," *Opt. Exp.*, vol. 19, pp. 25749–25762, 2011.
[15] J. M. Merlo, F. Ye, M. J. Burns, and M. J. Naughton, "Leakage radiation microscope for observation of non-transparent samples," *Opt. Exp.*, vol. 22, pp. 22895–22904, 2014.
[16] Y. Inouye and S. Kawata, "Near-field scanning optical microscope with a metallic probe tip," *Opt. Lett.*, vol. 19, pp. 159–161, 1994.
[17] F. Keilmann and R. Hillenbrand, "Near-field microscopy by elastic light scattering from a tip," *Trans. Roy. Soc. London. Ser. A: Math. Phys. Eng. Sci.*, vol. 362, pp. 787–805, 2004.
[18] F. Walla et al., "Anisotropic excitation of surface plasmon polaritons on a metal film by a scattering-type scanning near-field microscope with a non-rotationally-symmetric probe tip," *Nanophotonics*, vol. 7, pp. 269–276, 2018.
[19] K. J. Kaltenecker et al., "Mono-crystalline gold platelets: A high-quality platform for surface plasmon polaritons," *Nanophotonics*, vol. 9, pp. 509–522, 2020.
[20] E. Krauss et al., "Controlled growth of high-aspect-ratio single-crystalline gold platelets," *Cryst. Growth Des.*, vol. 18, pp. 1297–1302, 2018.
[21] R. Méjard et al., "Advanced engineering of single-crystal gold nanoantennas," *Opt. Mater. Exp.*, vol. 7, pp. 1157–1168, 2017.
[22] S. Boroviks et al., "Interference in edge-scattering from monocrystalline gold flakes," *Opt. Mater. Exp.*, vol. 8, pp. 3688–3697, 2018.
[23] G. Beane et al., "Surface plasmon polariton interference in gold nanoplates," *J. Phys. Chem. Lett.*, vol. 8, pp. 4935–4941, 2017.
[24] S. G. Menabde, J. T. Heiden, J. D. Cox, N. A. Mortensen, and M. S. Jang, "Image polaritons in van der Waals crystals," *Nanophotonics*, vol. 11, pp. 2433–2452, 2022.